




Ag-only inner electrode $\text{Na}_{0.5}\text{Bi}_{0.5}\text{TiO}_3$ -based X9R MLCC: achieving high performance and cost efficiency

Hamed Salimkhani^{1,*} , Lovro Fulanović¹, Marc Widenmeyer¹, and Till Frömling¹

¹ Department of Materials and Earth Science, Technical University of Darmstadt, Peter-Grünberg-Straße 2, 64287 Darmstadt, Germany

Received: 7 May 2024

Accepted: 29 August 2024

Published online:
23 September 2024

© The Author(s), 2024, corrected publication 2025

ABSTRACT

The demand for high-power electronic applications is set to drive the necessity for robust components like multi-layer ceramic capacitors (MLCCs). These MLCCs must endure a broad temperature range and withstand high electric fields. Simultaneously, the production cost of these components is a crucial concern for manufacturers. The regularly used Ag/Pd inner electrodes constitute the most significant cost factor. Hence, this study showcases the fabrication of a sodium bismuth titanate (NBT)-based MLCC using only Ag inner electrodes. This could be achieved by reducing the sintering temperatures with the help of sintering aids, but still maintaining excellent dielectric properties of the ceramic. This MLCC demonstrates an exceptional operational temperature range (−90 to 310 °C), high energy density (up to 5.1 J/cm³), higher efficiency (92%) at 217 kV/cm, and robust capacitance stability (variation less than 10%) even under high temperatures and electric fields.

Introduction

In recent years, considerable efforts have been made in the advancement of high-power applications. Especially, converting energy from renewable sources to electricity is driving the respective demand. Current conversion technology includes semiconductors, notably SiC and GaN Schottky diodes, alongside field-effect transistors (FET) such as metal oxide semiconductor field-effect transistors (MOSFETs) [1–3]. These semiconductors have showcased resilience and

dependability, particularly in demanding operational environments, withstanding temperatures of up to 300 °C and voltages reaching 1700 V [4]. In applications involving the conversion of AC voltage to DC through a rectifier, DC link capacitors are frequently utilized alongside these semiconductors to mitigate ripple voltage [4–7].

Various lead-based capacitors have shown promise [8] but have to be replaced due to the toxicity of lead posed by European Union [9]. As illustrated in Fig. 1, MLCCs feature stacks of alternating layers of dielectric

Handling Editor: David Cann.

Address correspondence to E-mail: Hamedsalimkhani25@gmail.com

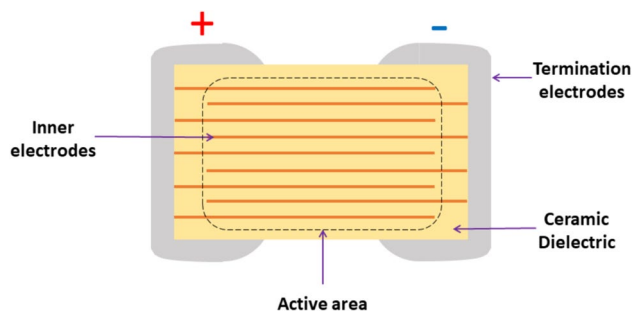


Figure 1 Schematic of an MLCC consisting of a dielectric material (yellow), inner electrodes (orange), and termination electrodes (gray).

materials and inner metal electrodes connected through external termination electrodes. They show high volumetric efficiency, proving effective in buffer, bypass, alternating-direct current conversion, filtering, and coupling-decoupling applications [10–19].

To meet the new industrial demand for alternative ceramic capacitor materials that operate across a wide range of temperatures from very low to high, and are capable of withstanding high electric fields different types of lead-free ceramic materials have been investigated [15, 20–22]. One commonly used MLCC in the market is based on BaTiO_3 (BT) material, which operates effectively only below 130 °C due to its lower Curie temperature [22–24]. Despite efforts to increase BT's Curie temperature to 200 °C, this improvement falls short of meeting the requirements for harsher environments (temperatures exceeding 200 °C) [25].

As a result, a new class of dielectrics with superior properties has emerged, categorized into two groups: potassium sodium niobate (KNN) [26–31] and sodium bismuth titanate (NBT) [32–37]. Among these, NBT shows promise for the respective capacitor applications [36]. However, integrating NBT solid solutions into industrial MLCC is challenging due to its sensitivity to oxygen vacancy formation during manufacturing, resulting in increased electrical conductivity and, thus, higher dielectric loss ($\tan \delta$) [35, 38–40]. Additionally, pristine NBT exhibits higher $\tan \delta$ at lower temperatures, elevated leakage current, and non-plateau permittivity (with variations exceeding $\pm 15\%$), thereby failing to meet the criteria for X7R, X8R, and X9R capacitors.

To tackle these challenges, prior research has utilized solid solutions of NBT with BT [41] and CaZrO_3 (CZ) [42]. The NBT-BT-CZ benchmark material

demonstrates a temperature-independent permittivity (up to 400 °C) and maintains low $\tan \delta$ (below 2%) up to a temperature of 350 °C.

Furthermore, recent prototype NBT-based MLCCs, though exhibiting impressive stability under varying temperature and electric field conditions, are hindered by their high cost attributed to the use of Pd or Pt as inner electrode materials [43–46]. To address this, a cost-effective alternative involves replacing these expensive electrode materials with more affordable options such as Ag. However, Ag's significantly lower melting point (961.8 °C) [47] compared to the sintering temperature required for NBT-BT-CZ [42] relaxor material necessitates a reduction in NBT's sintering temperature.

Our previous research has demonstrated that the utilization of specific sintering aids such as Li_2O , Bi_2O_3 , and B_2O_3 successfully reduces the sintering temperature of NBT-based solid solutions. Building upon this knowledge, our previous study delves deeper into the effects of these sintering aids on the high-temperature electrical properties of NBT-based solid solutions [48]. The findings unveil minimal adverse effects when these sintering aids are properly engineered.

Thus, this study leverages previous knowledge, enhancing NBT's electrical properties and lowering its sintering temperature, to enable the fabrication of MLCCs based on the NBT-BT-CZ benchmark material with Ag inner electrodes. The outcomes demonstrate outstanding temperature and voltage stability in these MLCCs, alongside excellent reliability and repeatability, underscoring their cost-effectiveness.

Experimental procedure

Synthesis

The synthesis of the $0.8(0.94[\text{Na}_{0.5}\text{Bi}_{0.5}\text{Ti}_{(1-x)}\text{Ta}_x\text{O}_3] - 0.06[\text{BaTi}_{(1-y)}\text{Ta}_y\text{O}_3]) - 0.2\text{CaZr}_{(1-z)}\text{Ta}_z\text{O}_3$, $x = y = z = 0.01$, composition was carried out using the conventional solid-state method. Before weighing the powders sourced from Alfa Aesar GmbH, Karlsruhe, Germany, Na_2CO_3 (99.5%), Bi_2O_3 (99.975%), BaCO_3 (99.8%), and CaCO_3 (99.5%) underwent drying at 300 °C. Simultaneously, TiO_2 (99.6%), ZrO_2 (99.5%), and Ta_2O_5 (99.85%) were dried at 800 °C because of their hygroscopic nature. The purity of the powders was also taken into consideration in the batch calculation. After precise weighing based on the stoichiometric formula,

the entire composition was placed in a nylon container filled with ethanol and subjected to 24 h of ball milling in a planetary mill (Pulverisette 5, Fritsch, Germany) at 250 rpm, using yttrium-stabilized zirconia balls. The resulting batch was transferred to a beaker and dried overnight at 100 °C. Next, the dried powder was moved to an alumina crucible and calcined at 900 °C for 3 h, with a heating rate of 5 °C/min. Following this, the calcined powder was milled for an additional 24 h in ethanol using zirconia balls at 250 rpm. After drying the slurries at 100 °C, a mixture of Li₂O, Bi₂O₃, and B₂O₃ was added into the main powder, with respective weight percentages of 0.100 wt%, 3.106 wt%, and 0.232 wt%. The procedure details are explained in our previous study [48].

MLCC fabrication

The process commenced by dispersing 61.84 wt% of the previously acquired powder into a solution consisting of 28.09 wt% methyl ethyl ketone (MEK, 99.5%, supplied by Carl ROTH GmbH, Karlsruhe, Germany) and 1.28% oleic acid as the dispersant. This dispersion was achieved using a planetary ball mill rotating at 100 rpm for approximately 4 h. Subsequently, 3.09 wt% polyethylene glycol (PEG 400, Alfa Aesar) was added as the plasticizer, followed by 5.70 wt% polyvinyl butyral (PVB, Mowital® LP BX 860) as the binder. The mixture underwent overnight milling to attain a homogeneous slurry suitable for tape casting. Tape casting was performed using an automatic machine (Proceq ZAA2300, Switzerland) equipped with adjustable speed and temperature, with a blade gap height set to 200 µm. After drying, tapes with a thickness of approximately 50 µm were obtained.

Subsequent to this, the dried tapes underwent screen printing using Ag paste (supplied by Gwent Group, UK), manual cutting, stacking, and pressing using a uniaxial press at a force of approximately 2 kN. Following this, the stacked tapes were subjected to debinding at 400 °C, with a heating rate of 1.0 °C/min and a dwell time of 2 h, resulting in tapes free of organic material. These tapes were then isostatically pressed at 700 kN and transferred to the furnace for sintering. To prevent any potential delamination of the stacks, the heat treatment commenced up to 600 °C at a heating rate of 1.0 °C/min, followed by a heating rate of 2.5 °C/min up to the sintering temperature (920 °C). A dwell time of 2 h was maintained at the sintering

temperature, after which the furnace was allowed to naturally cool down to room temperature.

Following sintering, the MLCCs underwent a heat treatment at 600 °C for 2 h. This step aimed to minimize the concentration of oxygen vacancies that are thermodynamically favored during the high-temperature sintering process. Subsequently, the obtained MLCCs were precisely cut and polished along the edges to expose their inner electrodes, facilitating the establishment of termination contacts. The sintered MLCCs had 5 layers with an active area of $\sim 1.5 \times 2.6 \text{ mm}^2$ and an inner dielectric layer thickness of 125 µm.

Characterization

The microstructure was assessed using a scanning electron microscope (SEM) equipped with energy-dispersive X-ray spectroscopy (EDX, X-Max80, Oxford Instruments, UK)—JEOL 7600, Japan. High-temperature permittivity (ϵ_r) and $\tan \delta$ data were obtained at 1 kHz through an LCR meter (4284A Precision LCR Meter, Hewlett Packard, USA) connected to a furnace (LE4/11/R6, Nabertherm GmbH, Germany). For low-temperature data (−115 to 50 °C), the measurements were performed using a Novocontrol Alpha-A High-Performance Frequency Analyzer (Novocontrol Technologies, Germany) and a Quatro Cryosystem (Novocontrol Technologies, Germany).

Impedance spectroscopy was carried out using the Novocontrol Alpha-A High-Performance Frequency Analyzer in the frequency range of 0.1 Hz to 3 MHz, with an amplitude of 0.1 V, covering temperatures from 125 °C to 600 °C. The resulting impedance data underwent analysis using RelaxIS software (rhd instruments, Germany). High-field measurements, including dielectric breakdown strengths, were conducted with a TF Analyzer 2000 (aixACCT Systems GmbH, Germany) in a temperature range of 25 °C–125 °C. The capacitance was measured with a small frequency of 1000 Hz and voltage amplitude of 25 V, which was superimposed to a unipolar triangular signal of 1 Hz, and the polarization was measured at 1 Hz in triangular signal mode. All samples probed with the TF Analyzer 2000 were immersed in silicone oil (AK 200, Wacker). Thermogravimetric analysis (TGA) was conducted with a NETZSCH STA 449C Jupiter, on the as-prepared tapes in an alumina crucible within air at a flow rate of 50 mL/min and a heating rate of 0.5–10 °C/min from room temperature

to 950 °C. The measurement was corrected for buoyancy. Optical images were captured using the Zeiss Axio Imager 2 microscope for cross-sectional analysis of the MLCCs.

Results and discussion

A higher solid load content of a tape significantly contributes to the density after sintering and, consequently, to the reliable and enhanced electrical properties of MLCCs. To verify whether the aimed solid content in the tape was achieved, we performed TGA

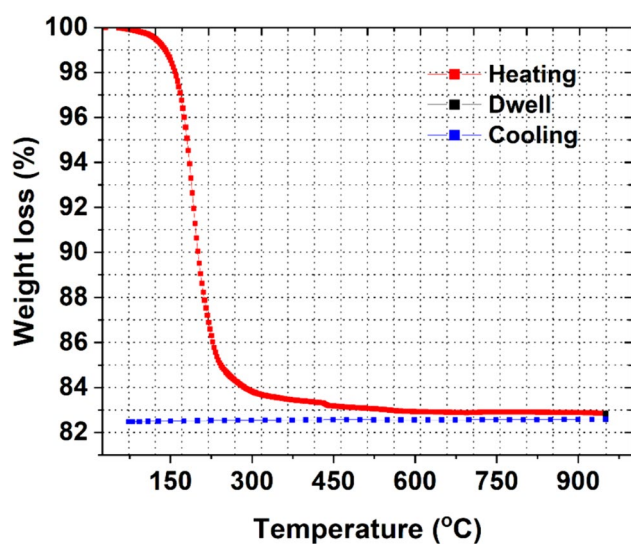


Figure 2 TGA graph of the as-prepared tape, showing the heating, dwell, and cooling stages in air.

analysis. Figure 2 shows the TGA results for a tape with an aimed powder content of 61.84 wt%. Once the tape is cast, the solvent content evaporates. Therefore, the observed weight loss in the figure pertains to a solvent-free tape. The majority of the weight loss happened between 62 °C and 450 °C. After normalization, the solid content was determined to be approximately 59 wt%, which is close to the target value. The remaining 2.84% discrepancy could be attributed to moisture absorbed by the powder during processing, which was likely evaporated during the TGA analysis.

During the sintering process, some Ag^+ ions may diffuse into the ceramic and act as dopants [49, 50]. It has been shown that Ag can diffuse up to 5 μm into BT during sintering [51]. Due to such a heavy diffusion, Ag ions can migrate, form dendrites, and short-circuit the layers under high electric fields. The challenge is that Ag probably acts as an acceptor dopant in NBT ceramics, which could increase the $\tan \delta$ and decrease the breakdown strength significantly. We conducted EDX mapping and line scans on the polished cross section (unetched) of the samples, as depicted in Fig. 3 to elucidate the elemental distributions. The mapping encompassed seven elements, including Na, Bi, Ti, Ba, Ca, Zr, and Ag. Figure 3 demonstrates that, within the detection limits of our device, no diffusion of Ag was observed. To closely examine the boundary between Ag and the dielectric, we conducted a line scan covering approximately 8 microns in total both before and after the Ag inner electrode. The results, presented in Fig. 4b, reveal no interdiffusion of Ag into the ceramic within the detection limit of our device, even in areas

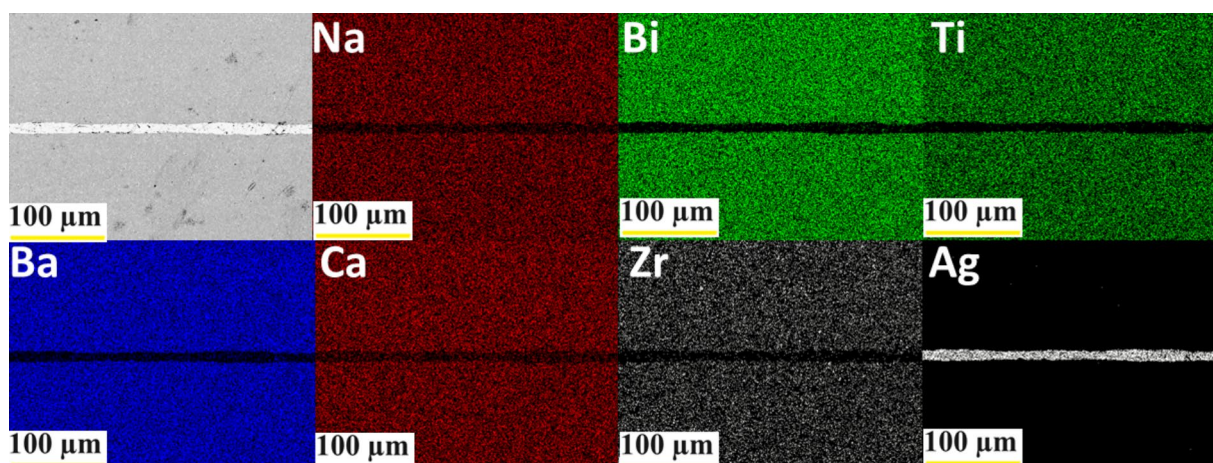


Figure 3 The EDX mapping of Ag/MLCC illustrates the distribution of its constituent elements, including Na, Bi, Ti, Ba, Ca, Zr, and Ag, showcasing the spatial arrangement of each element within the material.

Figure 4 **a** Photographs and dimensions of tested MLCCs. **b** The EDX line scan of a single layer of the Ag electrode and its vicinity to observe the potential diffusion of Ag into the dielectric material.

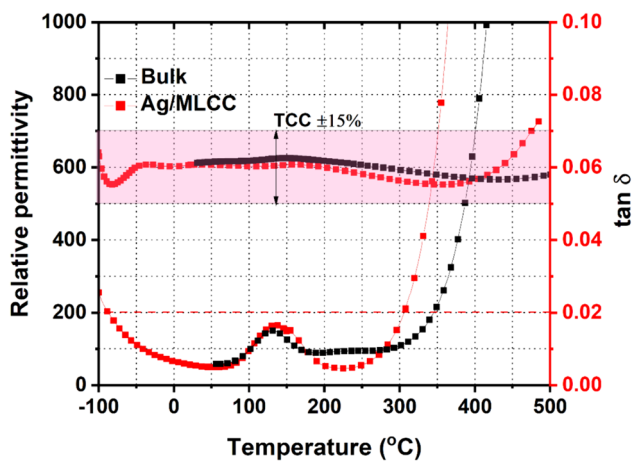
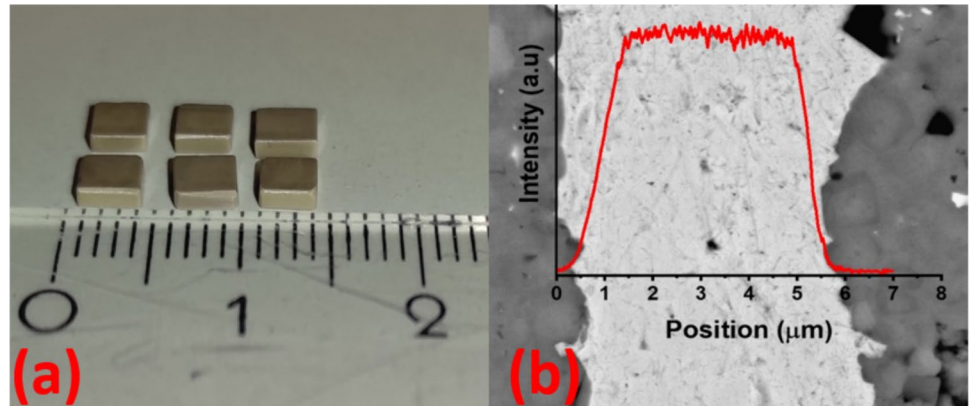


Figure 5 The temperature-dependent ϵ_r and $\tan \delta$ of bulk (positive temperature region) and Ag/MLCC (both in positive and negative temperature region) are depicted in the graph. The pink shaded area represents the variations of $\epsilon_r \pm 15\%$ of the bulk and MLCC, while the red dashed line indicates the maximum $\tan \delta$ threshold within which industrial capacitors typically operate.

proximate to the electrode. However, upon entering the electrode area, there is a sharp increase in the Ag concentration, evident from the red profile on the image in Fig. 4b. This does not necessarily imply that it is entirely absent, but rather that it has no significant impact on the properties and falls below the detection limit of the EDS method.

Figure 5 illustrates the temperature-dependent characteristics of a bulk and an Ag/MLCC, showcasing the relative permittivity (ϵ_r) and $\tan \delta$ at 1 kHz. For both bulk and Ag/MLCC samples, the ϵ_r exhibits a variation within the $\pm 15\%$ range (shown in the pink shaded area) over the temperature span of 25 °C–500 °C (bulk) and –100 °C to 474 °C (MLCC), a characteristic typical of capacitors classified as X9R

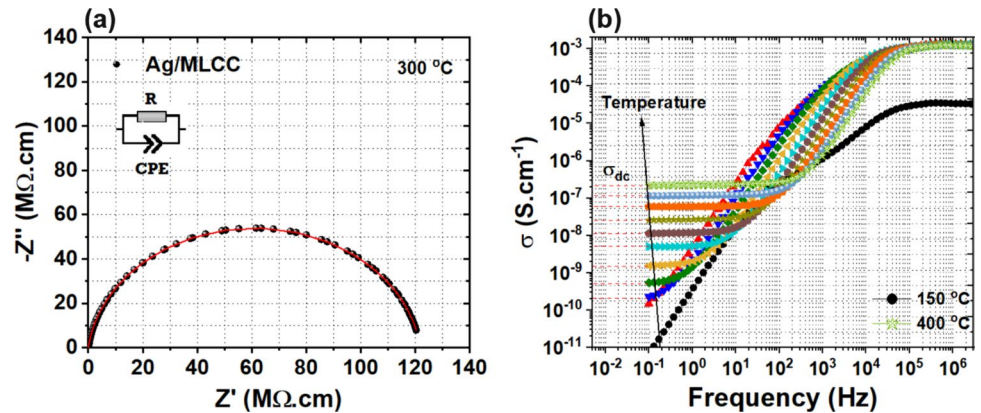
Table 1 The maximum ϵ_r , $\tan \delta$, and operational temperature window of Ag/MLCC at 1 kHz

Sample	Bulk	Ag/MLCC
ϵ_r (max)	635	618
$\Delta T(\epsilon_r \pm 15\%)$ (°C)	25–500	–100 to 474
$\Delta T(\tan \delta \leq 0.02)$ (°C)	25–350	–90 to 310
Frequency (Hz)	1000	1000

or higher [52]. Moreover, the $\tan \delta$ remains below 2% in the temperature range of 25 °C–350 °C for bulk (for low-temperature region the reader is referred to [43]) and –90 °C to 310 °C for Ag/MLCCs, surpassing the requirements for X9R capacitors and potentially qualifying for higher designation. The slight difference between the bulk and MLCCs may be attributed to the lower density of the MLCCs after sintering compared to bulk or to the slight diffusion of the Ag electrode into the dielectric material, which, however, could not be detected within the detection limit of our devices. The obtained results are comparable to the work of Ren et al. where they reported the $(1-x)\text{Na}_{0.5}\text{Bi}_{0.5+y}\text{TiO}_{3-x}\text{NaTaO}_3$ material system with Bi_2O_3 , CuO , Li_2CO_3 , ZnO , and B_2O_3 sintering aid composition [53]. Nevertheless, these results exceed those reported by Su et al. for an NBT-based X9R MLCC with Ag/Pd inner electrodes, where a temperature range of –55 to 205 °C was achieved with $\tan \delta$ remaining below 2% [52]. Such a stable plateau in ϵ_r is of paramount significance in circuit design for high-power SiC and GaN switching devices, providing designers with exceptional flexibility, such as the choice of voltage, temperature, and capacitance range. The summary of the data derived from this graph is provided in Table 1.

Figure 6a illustrates the Nyquist plot of the Ag/MLCC at 300 °C, spanning the frequency range of

Figure 6 **a** The Nyquist plot of the Ag/MLCC (black semicircle) fitted with an RC circuit (red semicircle) at 300 °C and **b** an approximation of DC conductivities in the temperature range of 150 °C to 400 °C calculated from the real part of impedance plots.

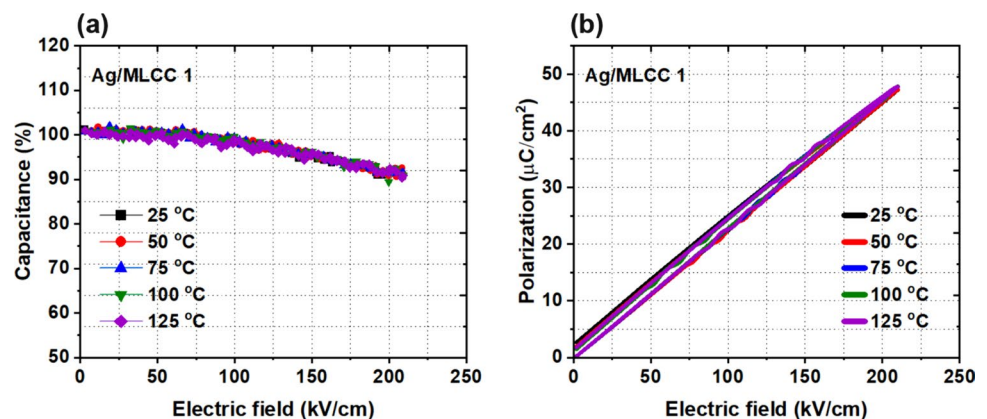


0.1 Hz to 3 MHz. The semicircle was fitted with a circuit containing a resistor denoted as R . To account for slightly non-ideal capacitive behavior a constant phase element (CPE) was paralleled with R . The careful analysis of the plot demonstrates only one semicircle response. Therefore, only bulk contribution, excluding grain boundary contribution, seems to dominate the electrical response. The fitting results showed a close to an ideal capacitor with an α value of 0.97. To further understand the DC conductivities (σ_{dc}) of Ag/MLCCs at various temperatures (in 25 °C increments), frequency-dependent σ_{ac} counterparts were plotted using the real component of the impedance as a function of frequency, and σ_{dc} values were then determined by extrapolating low-frequency conductivities to zero frequency similar to the work of Morozov et al. [54]. These values are depicted in Fig. 6b. As illustrated in the figure, at the operating temperature of 150 °C—aligned with the X8R capacitor classification—the σ_{dc} is remarkably low, measuring less than 10^{-11} S/cm. As the temperature increases, the conductivity correspondingly rises. For example, at the maximum operating temperature of the Ag/MLCC (~ 300 °C), the σ_{dc}

is estimated to be on the order of 10^{-8} S/cm which is comparable to the results of Xu et al. on $(1-x)(0.8\text{Na}_{0.5}\text{Bi}_{0.5}\text{TiO}_3-0.2\text{K}_{0.5}\text{Bi}_{0.5}\text{TiO}_3)-x\text{Bi}(\text{Mg}_{2/3}\text{Nb}_{1/3})\text{O}_3$ [55] and Fu et al. on $(1-x)(0.64\text{Na}_{0.5}\text{Bi}_{0.5}\text{TiO}_3-0.16\text{K}_{0.5}\text{Bi}_{0.5}\text{TiO}_3-0.20\text{Bi}(\text{Mg}_{2/3}\text{Nb}_{1/3})\text{O}_3)-x\text{CaZrO}_3$ [56] material systems.

Figure 7a, b illustrates temperature and field-dependent capacitance and polarization of Ag/MLCC. In Fig. 7a, it is evident that even with an electric field surpassing 200 kV/cm, the capacitance experiences only a slight decrease of 10%. This is a noteworthy accomplishment, as other ferroelectric (FE) or anti-ferroelectric (AFE) materials tend to exhibit a sharp decline or increase under such electric fields, respectively [57]. Even though the increase in AFE can be beneficial for obtaining a high energy density, a reliably field-independent behavior means better control over the electrical response for multiple applications. Moreover, within this electric field range, the capacitance remains temperature-independent up to the tested temperature (125 °C). Additionally, Fig. 7b reveals that the MLCCs exhibit a relaxor-type behavior with minimal $\tan \delta$ [58]. Similar to the capacitance-electric field relationship, a temperature-independent

Figure 7 Polarization vs. electric field of Ag/MLCC **a** at room temperature but with a higher maximum applied electric field and **b** at temperatures ranging from 25 °C to 125 °C with an increment of 25 °C at relatively lower electric fields.



correlation is observed for polarization vs. electric field. This underscores the robustness and reliability of the fabricated MLCCs.

Generally, the aim is to obtain capacitor properties that are frequency-independent over a large frequency range. Figure 8 illustrates the frequency-dependent capacitance of Ag/MLCCs across temperatures ranging from 150 °C to 400 °C, in 25 °C increments. As shown, increasing the temperature enhances the sensitivity of the MLCCs to frequency; while the capacitance exhibits a plateau at 150 °C, it transitions to a parabolic behavior at 400 °C within the frequency range of 0.1–100 kHz. Notably, at 1 kHz, the capacitance remains temperature-independent, even at 400 °C. The obtained results are much better than that of BT where the capacitance variation is significantly

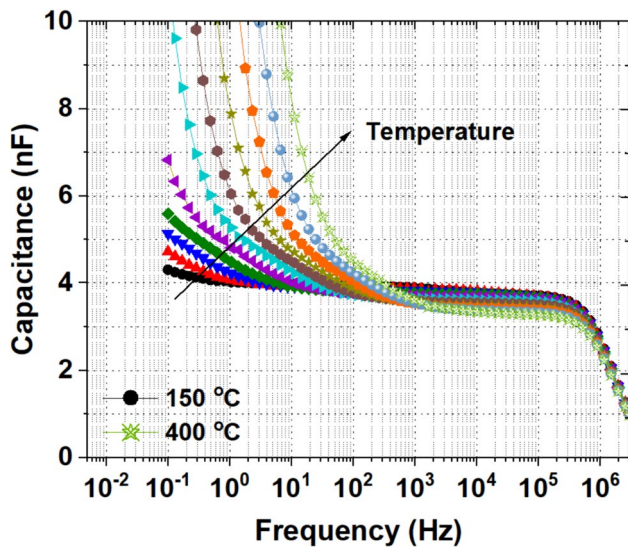
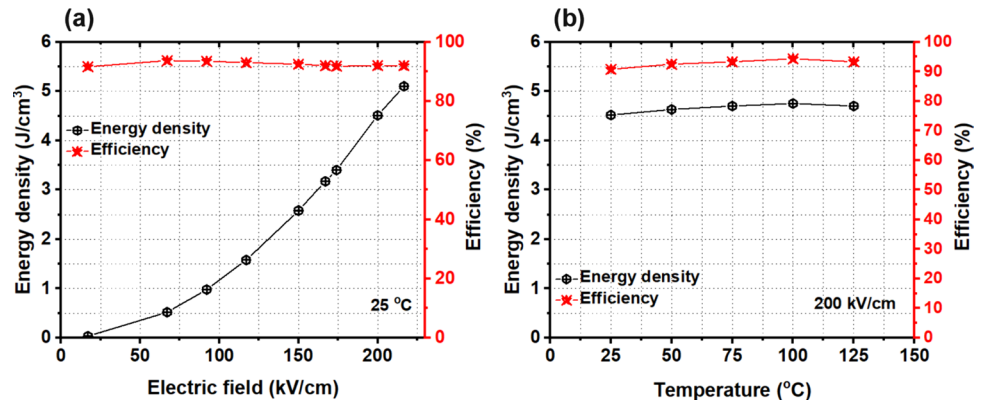


Figure 8 The frequency-dependent capacitance of Ag/MLCC at temperatures of 150 °C to 400 °C with an increment of 25 °C.

Figure 9 The energy density vs. **a** electric field at 25 °C and **b** temperature of Ag/MLCC at 200 kV/cm together with their relevant energy efficiencies are depicted.



higher [59]. Furthermore, the Ag/MLCCs demonstrate excellent capacitance stability, maintaining a value of approximately 4 nF at 150 °C up to a frequency of 100 kHz. The capacitance could be simply increased by increasing the number of active layers. Hence, with having the capacitance and DC resistance (obtained from Fig. 6b) available, the time constant ($\tau = RC$) was calculated to be 0.58 s at 175 °C.

The energy density (w_{total}) is a measure of the energy stored per unit volume in a ferroelectric material under an applied electric field. Energy density is calculated from polarization–electric field (P–E) loops (explained in supporting information). Figure 9a, b illustrates the computed energy densities and efficiencies plotted against the electric field and temperature, respectively. In Fig. 9a, it is evident that as the electric field increases, the energy density exhibits exponential growth, hitting 5.1 J/cm³ at 217 kV/cm. Moreover, the energy efficiency remains consistently high, exceeding 92% across all electric field values. Conversely, Fig. 9b demonstrates the response of energy densities to temperature variations. Remarkably, from 25 °C to 125 °C, both energy density and efficiency not only avoid decline but actually exhibit an increase, showcasing their robust performance across temperature fluctuations.

To further contextualize our findings, we compared them with the results of Gehringer et al., [43] who used Ag/Pd electrodes (notably more stable than bare Ag electrodes) and NBT-BT-CZ-based materials to construct MLCCs. Their study reported an energy density of approximately 1.1 J/cm³ and an efficiency of 92% at 220 kV/cm at room temperature (2.7 J/cm³ and 86% at 320 kV/cm). In contrast, our work achieved a significantly higher energy density of 5.1 J/cm³ with the same efficiency of 92% at 217 kV/cm at room

temperature. However, it is worth noting that their study demonstrated a higher dielectric breakdown strength than ours.

To ascertain the reliability of our MLCCs, we conducted tests on at least 5 samples for energy density, energy efficiency, and dielectric breakdown strength at room temperature. As depicted in Fig. 10a, four out of the five MLCCs exhibited energy densities surpassing 4.5 J/cm^3 , with MLCC4 reaching a maximum of 5.1 J/cm^3 before experiencing a breakdown. Furthermore, all MLCCs demonstrated energy efficiency exceeding 92%, underscoring the consistency and robustness of our fabricated MLCCs. Additionally, as illustrated in

Fig. 10b, the breakdown strength of the samples was evaluated. Four out of five samples exhibited dielectric breakdown strengths exceeding 200 kV/cm , with an average breakdown strength estimated to be 217 kV/cm . These results further validate the durability and performance of our MLCCs.

To shed light on the failure mechanisms underlying the breakdown of the MLCCs, we conducted cross-sectional analyses of several samples (Fig. 11a). As depicted in Fig. 11b, c, d, we identified primarily two distinct failure mechanisms.

One failure type originates from the edges of the MLCC (Fig. 11b). Consistent with findings from

Figure 10 Repeatability tests of the produced MLCCs. **a** The energy density and energy efficiency and **b** the dielectric breakdown strengths of the five produced MLCCs.

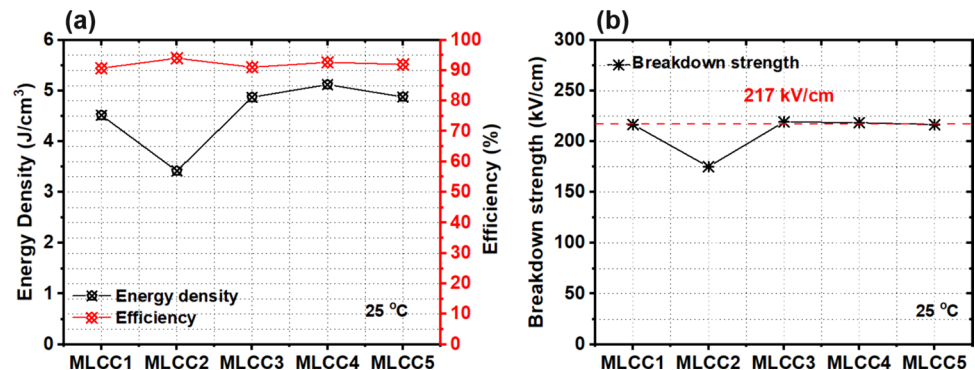
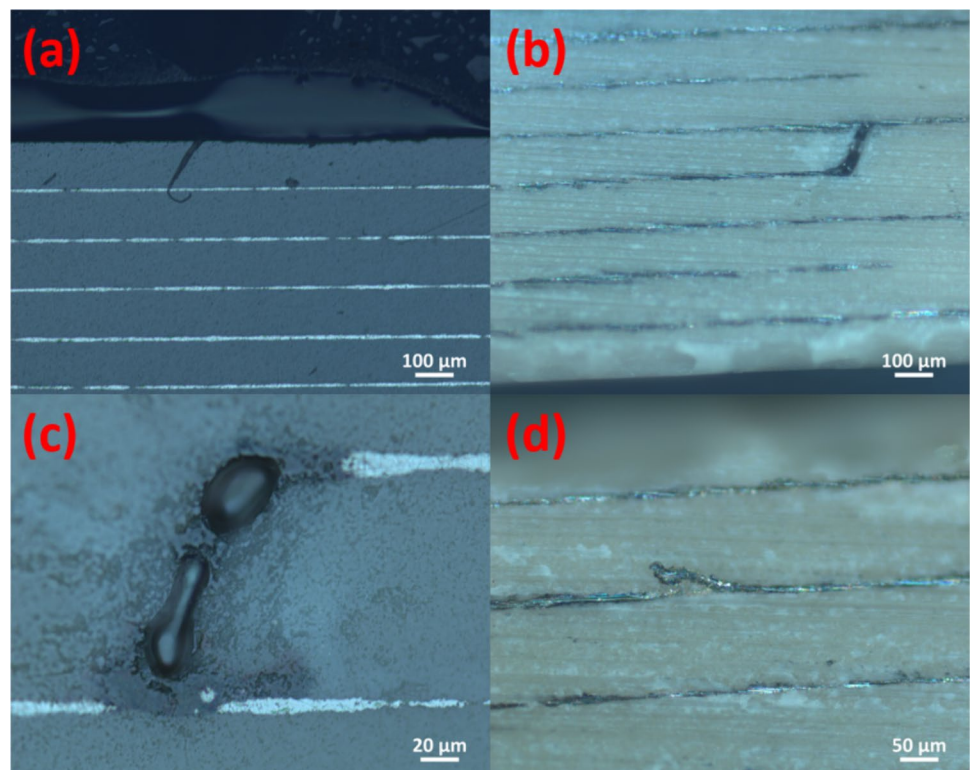


Figure 11 Optical cross-sectional images of Ag/MLCC demonstrating **a** an intact MLCC, **b** an MLCC failed through local enhancement of the field on the electrode tips, **c** magnified version of **b**, and **d** defects arising from electrode printing and processing.



previous studies [60, 61], we observed that electrode tips are particularly susceptible to failure due to the local field enhancements and charge accumulation in these regions [62]. The second failure mode stemmed from the center of the electrode, potentially linked to still present processing defects such as those occurring during electrode printing and processing. Thus, there is still some room for optimization toward industry relevant processes. However, our cross-sectional examinations revealed no instances of failure attributable to Ag-dendrite formation. That means that there is no material-related argument against implementing Ag-electrodes for NBT-based MLCC. Hence, being able to exclude Pd for NBT-based components is a large step toward reducing production cost.

Conclusion

Through meticulous engineering encompassing defect chemistry tailoring and sintering optimization in our previous study [48] and tailored slurry composition, tape casting, and MLCC design in this study, we successfully produced NBT-based high-power and high-temperature MLCCs with Ag inner electrodes. These are less costly and more environmentally friendly than Ag/Pd electrodes. The MLCCs demonstrate resilience to temperatures reaching 310 °C and electric fields of more than 200 kV/cm. Exposing the material up to 125 °C and high fields simultaneously did not impair the material either. Remarkably, high energy density of up to 5.1 J/cm³ and energy efficiency surpassing 92% at room temperature were achieved. Finally, high repeatability in properties such as energy density, energy efficiency, and dielectric breakdown strength showcased the robustness of the MLCCs. Furthermore, the microstructural analysis revealed no evidence of Ag interdiffusion into the dielectric material, while the observed failure modes aligned with those typical of MLCCs. Overall, this prototype MLCC with Ag-electrodes exhibits significant economically and industrially, laying the groundwork for the application of even more cost-effective electrode materials in future.

Acknowledgements

Hamed Salimkhani and Till Frömmling would like to thank the German Ministry of Education and Research (BMBF) for funding the Young Investigator Group

HTL-NBT within the program “NanoMatFutur” [Grant No. 03XP0146]. The authors are deeply grateful to the Nichtmetallisch-Anorganische Werkstoffe (NAW) group led by Prof. Jürgen Rödel for providing us with the opportunity to conduct experiments in their laboratories. We sincerely appreciate their support and generosity.

Funding

Open access funding enabled and organized by Projekt DEAL. Bundesministerium für Bildung und Forschung, 03XP0146, Till Frömmling

Supplementary Information The online version contains supplementary material available at <https://doi.org/10.1007/s10853-024-10174-w>.

Open Access This article is licensed under a Creative Commons Attribution-NonCommercial-No-Derivatives 4.0 International License, which permits any non-commercial use, sharing, distribution and reproduction in any medium or format, as long as you give appropriate credit to the original author(s) and the source, provide a link to the Creative Commons licence, and indicate if you modified the licensed material. You do not have permission under this licence to share adapted material derived from this article or parts of it. The images or other third party material in this article are included in the article’s Creative Commons licence, unless indicated otherwise in a credit line to the material. If material is not included in the article’s Creative Commons licence and your intended use is not permitted by statutory regulation or exceeds the permitted use, you will need to obtain permission directly from the copyright holder. To view a copy of this licence, visit <http://creativecommons.org/licenses/by-nc-nd/4.0/>.

References

- [1] Hornberger J, et al (2004) Silicon-carbide (SiC) semiconductor power electronics for extreme high-temperature environments. In: 2004 IEEE Aerospace Conference Proceedings (IEEE Cat. No. 04TH8720). IEEE
- [2] Neudeck PG, Okojie RS, Chen L-Y (2002) High-temperature electronics—a role for wide bandgap semiconductors? Proc IEEE 90(6):1065–1076

- [3] Shenai K, Scott RS, Baliga BJ (1989) Optimum semiconductors for high-power electronics. *IEEE Trans Electron Devices* 36(9):1811–1823
- [4] Lutz J et al (2011) *Semiconductor Power Devices: Physics, Characteristics, Reliability*. Springer Berlin Heidelberg, Berlin, Heidelberg. <https://doi.org/10.1007/978-3-642-11125-9>
- [5] Sarjeant WJ et al (1999) Capacitors—past, present, and future. *Handbook of Low and High Dielectric Constant Materials and Their Applications*. Elsevier, pp 423–491
- [6] Zubieta L, Bonert R (2000) Characterization of double-layer capacitors for power electronics applications. *IEEE Trans Ind Appl* 36(1):199–205
- [7] Ioinovici A (2001) Switched-capacitor power electronics circuits. *IEEE Circuits Syst Mag* 1(3):37–42
- [8] Meng X et al (2021) Systematical investigation on energy-storage behavior of PLZST antiferroelectric ceramics by composition optimizing. *J Am Ceram Soc* 104(5):2170–2180
- [9] Directive E (2013) Restriction of the use of certain hazardous substances in electrical and electronic equipment (RoHS). *Off J Eur Communities* 46:19–23
- [10] Kishi H, Mizuno Y, Chazono H (2003) Base-metal electrode-multilayer ceramic capacitors: past, present and future perspectives. *Jpn J Appl Phys* 42(1R):1
- [11] Lu Z et al (2020) Superior energy density through tailored dopant strategies in multilayer ceramic capacitors. *Energy Environ Sci* 13(9):2938–2948
- [12] Zhang H et al (2020) A review on the development of lead-free ferroelectric energy-storage ceramics and multilayer capacitors. *J Mater Chem C* 8(47):16648–16667
- [13] Sakabe Y (1997) Multilayer ceramic capacitors. *Curr Opin Solid State Mater Sci* 2(5):584–587
- [14] Hong K et al (2019) Perspectives and challenges in multilayer ceramic capacitors for next generation electronics. *J Mater Chem C* 7(32):9782–9802
- [15] Li J et al (2018) Multilayer lead-free ceramic capacitors with ultrahigh energy density and efficiency. *Adv Mater* 30(32):1802155
- [16] Wang G et al (2021) Electroceramics for high-energy density capacitors: current status and future perspectives. *Chem Rev* 121(10):6124–6172
- [17] Pan M-J, Randall CA (2010) A brief introduction to ceramic capacitors. *IEEE Electr Insul Mag* 26(3):44–50
- [18] Li J et al (2020) Grain-orientation-engineered multilayer ceramic capacitors for energy storage applications. *Nat Mater* 19(9):999–1005
- [19] Zhao Y, Meng X, Hao X (2021) Synergistically achieving ultrahigh energy-storage density and efficiency in linear-like lead-based multilayer ceramic capacitor. *Scripta Mater* 195:113723
- [20] Jayakrishnan A et al (2023) Are lead-free relaxor ferroelectric materials the most promising candidates for energy storage capacitors? *Prog Mater Sci* 132:101046
- [21] Wang G et al (2020) Fatigue resistant lead-free multilayer ceramic capacitors with ultrahigh energy density. *J Mater Chem A* 8(22):11414–11423
- [22] Zhao P et al (2021) Perspectives and challenges for lead-free energy-storage multilayer ceramic capacitors. *J Adv Ceram* 10:1153–1193
- [23] Jain A, Wang Y, Shi L (2022) Recent developments in BaTiO₃ based lead-free materials for energy storage applications. *J Alloy Compound* 928:167066
- [24] Li Y et al (2014) Significant increase of Curie temperature in nano-scale BaTiO₃. *Appl Phys Lett*. <https://doi.org/10.1063/1.4901169>
- [25] Zeb A, Milne S (2015) High temperature dielectric ceramics: a review of temperature-stable high-permittivity perovskites. *J Mater Sci Mater Electron* 26:9243–9255
- [26] Qu B et al (2017) Large recoverable energy storage density and low sintering temperature in potassium–sodium niobate-based ceramics for multilayer pulsed power capacitors. *J Am Ceram Soc* 100(4):1517–1526
- [27] Shao T et al (2017) Potassium–sodium niobate based lead-free ceramics: novel electrical energy storage materials. *J Mater Chem A* 5(2):554–563
- [28] Wu J, Xiao D, Zhu J (2015) Potassium–sodium niobate lead-free piezoelectric materials: past, present, and future of phase boundaries. *Chem Rev* 115(7):2559–2595
- [29] Yang Z et al (2016) Significantly enhanced recoverable energy storage density in potassium–sodium niobate-based lead free ceramics. *J Mater Chem A* 4(36):13778–13785
- [30] Zhang M et al (2022) Significant increase in comprehensive energy storage performance of potassium sodium niobate-based ceramics via synergistic optimization strategy. *Energy Storage Mater* 45:861–868
- [31] Zhou M et al (2018) Novel sodium niobate-based lead-free ceramics as new environment-friendly energy storage materials with high energy density, high power density, and excellent stability. *ACS Sustain Chem Eng* 6(10):12755–12765
- [32] Gomah-Pettry J-R et al (2004) Sodium-bismuth titanate based lead-free ferroelectric materials. *J Eur Ceram Soc* 24(6):1165–1169
- [33] Liu X et al (2018) Ultrahigh energy density and improved discharged efficiency in bismuth sodium titanate based relaxor ferroelectrics with A-site vacancy. *J Materiomics* 4(3):202–207

- [34] Wu Y et al (2019) Enhanced energy storage properties in sodium bismuth titanate-based ceramics for dielectric capacitor applications. *J Mater Chem C* 7(21):6222–6230
- [35] Yang F et al (2018) Defect chemistry and electrical properties of sodium bismuth titanate perovskite. *J Mater Chem A* 6(13):5243–5254
- [36] Yang H et al (2017) High energy storage density over a broad temperature range in sodium bismuth titanate-based lead-free ceramics. *Sci Rep* 7(1):8726
- [37] Yin J et al (2018) Ultrahigh energy-storage potential under low electric field in bismuth sodium titanate-based perovskite ferroelectrics. *J Mater Chem A* 6(21):9823–9832
- [38] Hiruma Y, Nagata H, Takenaka T (2009) Thermal depoling process and piezoelectric properties of bismuth sodium titanate ceramics. *J Appl Phys* 105(8):084112
- [39] Sung Y et al (2011) Effects of Bi nonstoichiometry in $(\text{Bi}_{0.5+x}\text{Na})\text{TiO}_3$ ceramics. *Appl Phys Lett* 98(1):012902
- [40] Carter J et al (2014) Structure and ferroelectricity of nonstoichiometric $(\text{Na}_{0.5}\text{Bi}_{0.5})\text{TiO}_3$. *Appl Phys Lett* 104(11):112904
- [41] Acosta M et al (2012) High-temperature dielectrics in CaZrO_3 -modified $\text{Bi}_{1/2}\text{Na}_{1/2}\text{TiO}_3$ -based lead-free ceramics. *J Eur Ceram Soc* 32(16):4327–4334
- [42] Höfling M et al (2018) Optimizing the defect chemistry of $\text{Na}_{1/2}\text{Bi}_{1/2}\text{TiO}_3$ -based materials: paving the way for excellent high temperature capacitors. *J Mater Chem C* 6(17):4769–4776
- [43] Gehringer M et al (2023) Prototyping $\text{Na}_{0.5}\text{Bi}_{0.5}\text{TiO}_3$ -based multilayer ceramic capacitors for high-temperature and power electronics. *J Eur Ceram Soc* 43(14):6122–6129
- [44] Jia W et al (2018) Superior temperature-stable dielectrics for MLCCs based on $\text{Bi}_{0.5}\text{Na}_{0.5}\text{TiO}_3$ - NaNbO_3 system modified by CaZrO_3 . *J Am Ceram Soc* 101(8):3468–3479
- [45] Zhao Y et al (2022) Enhanced energy-storage properties in $\text{Bi}_{0.5}\text{Na}_{0.5}\text{TiO}_{3-x}\text{Sr}_{0.85}\text{Bi}_{0.1}\text{TiO}_3$ by regulating relaxation temperature and constructing multilayer structure. *Mater Sci Eng B* 282:115773
- [46] Ren P et al (2023) Super-stable permittivity and low dielectric loss of $(1-x)\text{Na}_{0.5}\text{Bi}_{0.5+y}\text{TiO}_{3-x}\text{NaTaO}_3$ ceramics within an ultra-wide temperature range. *J Materiomics* 9(3):482–491
- [47] Holman S, Lawrence R, Barr L (1895) Melting points of aluminum, silver, gold, copper, and platinum. In: *Proceedings of the American Academy of Arts and Sciences*. JSTOR
- [48] Salimkhani H, Fulanović L, Frömling T (2024) Sinterability of sodium bismuth titanate-based electroceramics at low temperatures. *J Eur Ceram Soc* 44(3):1570–1580
- [49] Andrejs L, Fleig J (2013) Resistance degradation in donor-doped PZT ceramic stacks with Ag/Pd electrodes: I. Phenomenology of processes. *J Eur Ceram Soc* 33(4):779–794
- [50] Andrejs L et al (2013) Resistance degradation in donor-doped PZT ceramic stacks with Ag/Pd electrodes: II. Distribution of conduction paths. *J Eur Ceram Soc* 33(6):1165–1176
- [51] Shih SJ, Tuan WH (2004) Solubility of silver and palladium in BaTiO_3 . *J Am Ceram Soc* 87(3):401–407
- [52] Su C et al (2016) Manufacture and dielectric properties of X9R Bi-based lead-free multilayer ceramic capacitors with AgPd inner electrodes. *J Mater Sci Mater Electron* 27:6140–6149
- [53] Ren P et al (2023) Super-stable permittivity and low dielectric loss of $(1-x)\text{Na}_{0.5}\text{Bi}_{0.5+y}\text{TiO}_{3-x}\text{NaTaO}_3$ ceramics within an ultra-wide temperature range. *J Materiomics* 9(3):482–491. <https://doi.org/10.1016/j.jmat.2022.12.004>
- [54] Morozov MI, Damjanovic D (2010) Charge migration in $\text{Pb}(\text{Zr,Ti})\text{O}_3$ ceramics and its relation to ageing, hardening, and softening. *J Appl Phys*. <https://doi.org/10.1063/1.3284954>
- [55] Xu Y et al (2020) Superior ultra-high temperature multilayer ceramic capacitors based on polar nanoregion engineered lead-free relaxor. *J Eur Ceram Soc* 40(13):4487–4494
- [56] Fu Y et al (2022) Construction of lead-free dielectrics for high temperature multilayer ceramic capacitors and its inner electrode matching characteristics. *J Alloy Compd* 903:163995
- [57] Kainz T et al (2016) Comparison of lanthanum and bismuth modification of lead zirconate-lead titanate PZT—a structural and dielectric study. *J Eur Ceram Soc* 36(3):507–514
- [58] Yuan Q et al (2017) Relaxor ferroelectric 0.9BaTiO_3 - $0.1\text{Bi}(\text{Zn}_{0.5}\text{Zr}_{0.5})\text{O}_3$ ceramic capacitors with high energy density and temperature stable energy storage properties. *J Mater Chem C* 5(37):9552–9558
- [59] Reddy YV, Mergel D (2007) Frequency and temperature-dependent dielectric properties of BaTiO_3 thin film capacitors studied by complex impedance spectroscopy. *Physica B* 391(2):212–221
- [60] Weachock R, Liu D (2013) Failure analysis of dielectric breakdowns in base-metal electrode multilayer ceramic capacitors. TX, USA, CARTS International. Houston, pp 25–28
- [61] Teverovsky A (2019) Cracking problems in low-voltage chip ceramic capacitors
- [62] Samantaray MM et al (2012) Electrode defects in multilayer capacitors part I: modeling the effect of electrode roughness and porosity on electric field enhancement and leakage current. *J Am Ceram Soc* 95(1):257–263

Publisher's Note Springer Nature remains neutral with regard to jurisdictional claims in published maps and institutional affiliations.